



LAWRENCE
LIVERMORE
NATIONAL
LABORATORY

First-principles high-pressure unreacted equation of state and heat of formation of crystal 2,6-diamino-3,5-dinitropyrazine-1-oxide (LLM-105)

M. R. Manaa, I. W. Kuo, L. E. Fried

May 19, 2014

Journal of Chemical Physics

Disclaimer

This document was prepared as an account of work sponsored by an agency of the United States government. Neither the United States government nor Lawrence Livermore National Security, LLC, nor any of their employees makes any warranty, expressed or implied, or assumes any legal liability or responsibility for the accuracy, completeness, or usefulness of any information, apparatus, product, or process disclosed, or represents that its use would not infringe privately owned rights. Reference herein to any specific commercial product, process, or service by trade name, trademark, manufacturer, or otherwise does not necessarily constitute or imply its endorsement, recommendation, or favoring by the United States government or Lawrence Livermore National Security, LLC. The views and opinions of authors expressed herein do not necessarily state or reflect those of the United States government or Lawrence Livermore National Security, LLC, and shall not be used for advertising or product endorsement purposes.

First-principles high-pressure unreacted equation of state and heat of formation of crystal 2,6-diamino-3, 5-dinitropyrazine-1-oxide (LLM-105)

M. Riad Manaa^{*}, I-Feng W. Kuo, and Laurence E. Fried

Lawrence Livermore National Laboratory, Energetic Materials Center,
Livermore, CA, 94551

^{*} Corresponding author, email: manaa1@llnl.gov

Abstract

We report dispersion-corrected density functional theoretical calculations of the unreacted equation of state (EOS) of crystal 2,6-diamino-3, 5-dinitropyrazine-1-oxide (LLM-105) under hydrostatic compression of up to 45 GPa. Convergence tests for k -points sampling in the Brillouin zone show that a $3 \times 1 \times 2$ mesh is required to reproduce the X-ray crystal structure at ambient conditions, and we confirm our finding with a separate supercell calculation. Our high-pressure EOS yields a bulk modulus of 19.18 GPa, and indicates a tendency towards anisotropic compression along the b lattice vector due to molecular orientations within the lattice. We find that the electronic energy band gap decreases from a semiconductor type of 1.3 eV at 0 GPa to quasi-metallic type of 0.6 eV at 45 GPa. The extensive intermolecular hydrogen bonds involving the oxide (-NO) and dioxide (-NO₂) interactions with the amine (-NH₂) group showed enhanced interactions with increasing pressure that should be discernible in the mid IR spectral region. We do not find evidence for structural phase transitions or chemically induced transformations within the pressure range of our study. The gas phase heat of formation is calculated at the G4 level of theory to be 22.48 kcal/mol, while we obtain 25.92 kcal/mol using the ccCA-PS3 method. Density functional theory calculations of the crystal and the gas phases provided an estimate for the heat of sublimation of 32.4 kcal/mol. We thus determine the room-temperature solid heat of formation of LLM-105 to be -9.9 or -6.5 kcal/mol based on the G4 or ccCA-PS3 methods, respectively.

I. Introduction

In a quest for safe and yet highly energetic explosive materials, the molecule 2,6-diamino-3, 5-dinitropyrazine-1-oxide (designated as LLM-105 for Lawrence Livermore Molecule #105, Figure 1a) was recently synthesized as a potential high-performance/low-sensitivity candidate.¹ This material is a highly dense molecular solid ($\rho = 1.92 \text{ g/cm}^3$) that crystallizes in a monoclinic, $P2_1/n$ space symmetry group, with four molecules per unit cell (Figure 1b), as was determined by single crystal X-ray diffraction.² Similar to the highly insensitive explosive 1, 3, 5-triamino-2, 4, 6-trinitrobenzene (TATB),^{3,4} LLM-105 exhibits an extensive network of both intra- and intermolecular hydrogen bonds, which could be responsible for its high stability. Thermal and shock sensitivity measurements, and subsequent ignition and growth modeling of a plastic bonded explosive formulation (92.4% LLM-105 and 7.6% Kel-F binder) established LLM-105 as an intermediate between the less energetic, insensitive explosive TATB and the more energetic, sensitive explosive HMX (octahydro-1,3,5,7-tetranitro-1,3,5,7-tetrazine).^{5,6} A calculated detonation velocity of 8529 m/s, detonation pressure of 31.44 GPa, and adiabatic time to explosion of 873.3 seconds at $T=298.15 \text{ K}$ have been reported for this explosive material based on quantum chemical calculations and Micro-DSC measurements.⁷ Its thermal stability up to 513 K at ambient pressure was also experimentally established.⁸

Macroscopic simulations of the shock wave initiation of explosive materials utilize reactive flow models that require, among others, accurate determination of the unreacted equation of state (EOS) up to 1.5 times the Chapman-Jouguet pressure (roughly 45 GPa for LLM-105). The isothermal pressure vs. volume EOS (P-V curve)

provides a thermodynamic relationship fundamental to such equation of state models. Unfortunately, experimental determinations of the P-V EOS do not usually encompass the entire pressure range of interest in the detonation process (0 - 45 GPa). Such important regions as the Von Neumann spike and the Chapman-Jouguet state of complete reactivity are in the high pressures and/or temperatures regimes, and difficult to access with diamond anvil cell methods. First-principles atomistic calculations with density functional theory (DFT) have become viable in obtaining these crucial data. The use of proper functional,⁹ the inclusion of long-range van der Waals dispersion forces for systems with strong hydrogen bonding,¹⁰⁻¹² and the careful selection of appropriate k-point mesh in the Brillouin zone,¹³ are all crucial variables for producing accurate EOS results.

Two very recent studies have investigated the phase stability of LLM-105. In an experimental investigation, Gump et al. used synchrotron angle-dispersive x-ray diffraction and diamond anvil cells to determine isothermal equations of state of LLM-105 at static high-pressure and temperature.⁸ P-V relations were obtained at temperatures of 298, 373, and 453 K for pressures of up to 5.5 GPa. Third-order Birch-Murnaghan EOS fits of these data provided bulk moduli of 11.19, 4.61, and 0.74 GPa, respectively. The study concluded that no phase change was evident up to the highest measured pressure.

In a computational study, pure (i.e. without dispersion correction) DFT calculations were performed on crystal LLM-105 under hydrostatic pressure up to 50 GPa.¹⁴ Optimization of the crystal structure at ambient conditions using the generalized gradient approximation and the Perdew-Wang 91 functional (GGA/PW91) yielded large

errors (26.9% for cell volume) when compared with the experimentally determined structure. The local density approximation treatment (LDA) yielded a seemingly better result for the crystal structure, a not altogether surprising conclusion based on previous LDA studies of energetic systems.¹⁵⁻¹⁷ The authors investigated the effect of high-pressure on the geometric, electronic and absorption properties of LLM-105, and reported four structural transformations at 8, 17, 25, and 42 GPa due to calculated irregularities in cell parameters and the band gap of the crystal.

In this work, we use dispersion-corrected DFT calculations to study the hydrostatic compression of crystal LLM-105 up to 45 GPa. We show that by also choosing a sufficiently dense k-point mesh of integration points, the GGA method provides an optimized crystal structure that is in very good agreement with experiment. This allows us to construct an accurate unreacted EOS up to the calculated pressure. We determine that under pressure LLM-105 transitions from a semi-conductor to a quasi-metal at higher pressure. The inclusion of dispersion forces in our calculations allows us to examine the effect of pressure on inter-molecular hydrogen bonds. We also conduct room-temperature constant pressure molecular dynamics simulation ($P=0.0$ GPa) of the solid to compare with experimental results. Using DFT and composite quantum chemical calculations, we provide an estimate of the heat of formation of solid LLM-105.

II. Computational Approach

The reported calculations were performed using two different approaches, both utilizing DFT within the generalized gradient corrected approximation of Perdew–Burke–Ernzerhof (PBE) for the exchange-correlation potential,¹⁸ and the inclusion of the DFT two-body (D2) dispersion correction as proposed by Grimme.¹⁰ The first approach was

used to investigate the equilibrium crystal structure and its associated electronic structure calculations of band structure and density of state (DOS), and establish the convergence of the reciprocal space integration. The second, supercell approach within the gamma point formulation was used to produce the high pressure EOS and for molecular dynamics simulations.

In the first approach, the orbitals were expanded in a plane wave basis set, and the electron-ion interactions were described by Vanderbilt-type ultrasoft pseudopotentials.¹⁹ We chose a plane wave basis with a kinetic energy cutoff of 700 eV, which was found to produce acceptable results based on several preliminary test calculations. Wavefunctions were determined using the Pulay density-mixing minimization scheme for the self-consistent field calculations,²⁰ while structure optimizations were performed with the BFGS (for Broyden, Fletcher, Goldfarb, and Shanno) method.²¹ Our k-point convergence test included 3 different sets of Brillouin zone sampling, performed by applying the Monkhorst-Pack scheme with k-point grids of 2x1x2, 3x1x2, and 6x2x4 along the a, b, and c reciprocal axes.¹³ Sufficiently stringent structure and cell optimization convergence criteria were implemented: total energy was converged to a tolerance of less than 1×10^{-5} eV/atom, the residual forces to less than of 0.03 eV/Å, the residual stress to less than 0.05 GPa, maximum displacement to less than 0.001 Å, and the self-consistent field convergence criterion of 5×10^{-7} eV/atom. A single, periodic unit cell, which contains four LLM-105 molecules (76 atoms) was used in this approach starting from the experimental crystal structure of Gilardi and Butcher,² and without any symmetry constraints during the optimization procedure. The calculations were performed at this level of computation using the CASTEP program.²² This approach was

used to obtain the equilibrium crystal structure lattice parameters and calculate the partial (s and p) and total density of states (DOS).

In the second approach, a dual basis set formalism was used for the description of wavefunctions and electron density. A triple zeta with double polarization (TZV2P) Gaussian type orbital basis was utilized for the wavefunctions, while plane wave basis expanded to 320 Ry was used to represent the electron density. The core electronic states were represented by the norm conserving Goedecker-Teter-Hutter pseudopotentials.²³ All convergence criteria implemented in the first approach as specified above have also been adapted in the second approach. We used several supercells varying in size for calculations of the crystal equilibrium structure (without any symmetry constraints), while production runs for the high-pressure EOS and the molecular dynamics simulation were based on a 3x1x2 supercell, which contained 24 LLM-105 molecules (456 atoms). The isobaric-isothermal molecular dynamics simulation was carried out following the recipe outlined by Schmidt et al.²⁴ The wavefunctions were explicitly minimized to 10^{-7} Hartree using the orbital transformation method for every dynamics step.²⁵ Forces were then utilized to propagate the molecular dynamics simulation in the isobaric ensemble (NPT) with a fixed time step of 0.5 fs. Simulations were conducted at T=300 K, with temperature being controlled via individual Nosé-Hoover chains coupled to each degree of freedom using a coupling constant of 2000 cm^{-1} .^{26,27} The barostat coupling parameter was 500 fs. The calculations were performed using the Quickstep module within the CP2K simulation suite.^{28,29}

Finally, the calculation of the gas-phase (single molecule) heat of formation of LLM-105 was carried out at the Gaussian-4 level of theory (G4),³⁰ as implemented in the

Gaussian 09 code.³¹ Gas phase calculations were also performed using the CCCA-PS3 composite thermochemical method,^{32, 33} with individual calculations performed in parallel using the GAMESS thermochemical code.³⁴ Unlike the G4 method, the ccCA-PS3 method has no adjustable parameters fit to experimental heats of formation. Its overall accuracy, however, is similar to that of the G3 method.³⁵

III. Results and Discussion

A. Equilibrium Crystal Structure.

Complete optimization of the LLM-105 unit cell provided the structure parameters reported in Table I. They are compared with the x-ray experimental result² and the recent computational study.¹⁴ First, we note the difference between the results of k-point meshes 2x1x2 and 3x1x2, which produce some deviations in lattice parameters: 0.08 Å in a , 0.09 Å in b , 0.06 Å in c , and 0.77° in the angle β . Second, the results of the 3x1x2 and 6x2x4 k point meshes, however, are almost identical, with deviation of 0.003 and 0.001 Å in the parameters b and c , respectively, also reflecting the almost identical value for the cell volume. These results clearly show that the 3x1x2 k-point grid is a good representation of the Brillouin zone, as convergence has been attained. The computed lattice parameters with this k-point treatment show very good agreement with the experimental determination reproduced in the table, with deviations being 0.015 Å in a (0.3%), 0.129 Å in b (0.8%), 0.021 Å in c (0.25%), 0.39° in β (0.4%), and 5.1 Å³ (0.7%) in the cell volume.

The supercell calculations confirmed that a single unit cell (1x1x1) optimization is completely inadequate when compared with the experimental results, yielding an error

as large as 3.73 Å in the b parameter (23.6%), as reported in the table. The optimal results are obtained with the 3x1x2 supercell, yielding the smallest deviations from the experimental determination: 0.002 Å in a (0.03%), 0.123 Å in b (0.8%), 0.000 Å in c (0.0%), 0.23° in β (0.2%), and 0.01° in γ . The accuracy of these results is remarkable, considering the absence of a computed temperature effect, as the experimental data was recorded at T=298 K.² We also note that even though increasing the size to a 6x2x4 supercell does not necessarily provide more accurate results when compared with the experimental data, convergence within this supercell Γ -point treatment is also achieved.

The recent DFT results of Wu et al.,¹⁴ also reproduced in Table I, showed poor agreement with experimental data at the GGA/PW91 level of computation, while relatively better results are achieved with the lower level of local density approximation (LDA). In the reported study, a k-point mesh of 2x1x2 was used and no dispersion correction was implemented. This may explain the drastic error in the GGA/PW91 results (~27% for cell volume), aside from the validity of the PW91 functional for this system. That the lower theoretical level LDA treatment produced better results despite the lack of dispersion correction or a higher k-point mesh, is not indicative of the accuracy or adequacy of this method, as our results clearly show dependency on suitable sampling representation in the Brillouin zone. We note that a comparative DFT study for TATB also showed better agreement with experiment from LDA than from the generalized gradient approximation (GGA) with neglect of dispersion forces and convergence tests for k-points grids.¹⁵ Most likely the well-known overbonding behavior found with LDA partly compensates for the lack of dispersion interaction in prior calculations.³⁶

Figure 2 shows the calculated contribution from s and p states as well as the total density of state (DOS) of the equilibrium crystal structure from the 3x1x2 k-point scheme. Near the Fermi level, p states are dominant in the valence and conduction bands in the range -1 to 5 eV. The calculated indirect band gap is 1.42 eV, which suggests that LLM-105 may have semiconductor-like band gap, unlike many other molecular solid energetic materials with insulator type (> 2.5 eV) band gaps such as TATB,¹⁶ HMX,³⁷ or PETN.³⁸ This conclusion must, however, be qualified by the high errors sometimes found in band gaps calculated by DFT.³⁹ Orbital analysis showed that the highest occupied molecular orbital (HOMO), doubly-degenerate, is mainly localized on the oxide (N-O). The lowest occupied molecular orbital (LUMO), with similar degeneracy, is a π orbital associated with the NO₂ moieties. In absolute energy terms, the HOMO of LLM-105 is higher in energy than that encountered in TATB, an orbital that is associated with C-C-C conjugate bonds within the benzene ring. Since the LUMO in nitro-containing compounds is similarly located on the NO₂, the reduction of the band gap in LLM-105 is due to the higher energetic shift of the HOMO. The supercell calculations reported herein also determined a HOMO-LUMO separation of 1.30 eV at the zero pressure equilibrium structure. Undoubtedly, experimental measurements of the actual band gap of this material would be most appropriate to establish if LLM-105 could be added to a growing list of organic semiconductors.⁴⁰

Finally, we also determined the unit cell volume at ambient conditions via a constant isobaric-isothermal molecular dynamics run up to ~ 14 ps. Figure 3 displays the temporal profiles of the dominant, diagonal stress components P_{xx} , P_{yy} , and P_{zz} , the temperature ($T=300$ K), and the cell volume. In addition to the resulting raw data shown

in the figure, 1ps and 2ps running block run-averages are plotted so as to indicate the system is in equilibrium. As shown, all three stress components are at steady state at 0.0 GPa, and the temperature is uniform at 300K. The resulting unit cell volume from the last block average of the simulation is 769.3 \AA^3 (4615.8 \AA^3 for the simulation $3 \times 1 \times 2$ supercell, as in the figure). This value compares well with the experimental measurement of Gump et al. at $298 \pm 2 \text{ K}$, which records a volume of $747.7 \pm 1.18 \text{ \AA}^3$.⁸ We note that vibrational quantum effects (zero-point energy) have not been taken into accounts in the Newtonian dynamics of our simulation.

B. High-Pressure Behavior.

The calculated P - V isotherm up to 6 GPa, along with the experimental determinations of Gump et al.⁸ are shown in Figure 4a, while the calculated isotherm in the entire pressure range up to 45 GPa is shown in Figure 4b. We note that the calculated EOS in Figure 4a compares well with the experimental data, which included error bars not reproduced here, and despite the neglect of temperature effects in the calculated EOS. A slight stiffness of the calculated EOS can be noted in the low- pressure range $\leq 1 \text{ GPa}$.

Fitting the calculated P - V compression data to the third-order Birch-Murnaghan equation of state (EOS):⁴¹

$$P = \frac{3B_0}{2} \left[\vartheta^{7/3} - \vartheta^{5/3} \right] \times \left[1 + \frac{3}{4} (B'_0 - 4) \left(\vartheta^{2/3} - 1 \right) \right],$$

where $\vartheta = \frac{V_0}{V}$, and $B_0 = -V \left(\frac{\partial P}{\partial V} \right)$, allow us to determine the bulk pressure modulus (B_0) and its pressure derivative (B'_0). In the above equation, V_0 is the zero-pressure volume, calculated to be 742.66 \AA^3 (as in Table I). We fit our data in two pressure ranges. Up to $P=6 \text{ GPa}$, we found $B_0 = 17.37 \pm 1.44 \text{ GPa}$ and $B'_0 = 7.89 \pm 1.34$. Fitting the entire P - V

curve up to 45 GPa yielded $B_0 = 19.18$ GPa and $B'_0 = 7.22$. The second fit is shown as the solid line in Figure 4b. These results are compared with the experimental fits that were recorded at ambient temperature in Table II. The deviation between these results in the pressure region < 5.5 GPa indicates stiffness in the calculated EOS, and perhaps is indicative of the importance of temperature inclusion for structural relaxation effects. The experimental measurements clearly showed that LLM-105 becomes more compressible at higher temperatures (373 and 453 K).⁸

Figures 5 and 6 show the pressure dependence of the calculated lattice parameters a (Fig.5a), b (Fig.5b), c (Fig.5c), and the angles α and γ (Fig.6a), and β (Fig.6b). The experimental parameters a , b , and c are shown in Figure 5 for the measured pressure regime < 6 GPa. These parameters compare well with the calculated ones with maximum deviation of about 0.05 Å. The initial steep decrease with increasing pressure in the range of 0-6 GPa indicates an enhanced tendency of LLM-105 to be more compressible in this pressure range. The calculated pressure dependence of these parameters up to 45 GPa shows a decrease with increasing pressure from 5.71 to 5.08 Å for a , from 15.73 to 12.36 Å for b , and from 8.41 to 7.43 Å for c . These correspond to 11%, 21%, and 11.6% reduction from the equilibrium geometry of these constants, respectively, and indicating an anisotropic compressibility of LLM-105 in the b direction. The higher compressibility in the b direction can be attributed to the molecular orientations within the unit cell (see Figure 1b) where repulsion between neighboring atoms is weaker than in the a and c directions.

The unit cell of LLM-105 is monoclinic at ambient conditions, with α and γ being 90°. Figure 6a shows that there are pressure regions where symmetry is broken and the

lattice transitions to triclinic type. The deviation of these two angles from 90° is very small, as shown in the Figure, with maximum changes being -0.3 and $+0.2$ degrees. Nonetheless, this symmetry breaking is important in providing more degrees of freedom for the system to relax under pressure. We note that in the pressure regimes 19-25 and 30-45 GPa the lattice reverts to being of monoclinic type. Figure 6b shows the fluctuation of the β angle with pressure between the two extrema 101.8° at 1 GPa and 98.4° at 39 GPa. LDA calculations showed a reverse effect, an increase of β with increasing pressure from $\sim 99.5^\circ$ to $\sim 104^\circ$.¹⁴ These non-uniform fluctuations with pressure are also present in all other lattice parameters of Figure 5. Pressure increases in a [at 5, 9, 16, 19, 22, 28, and 32 GPa], in b [at 14, 20, 27, 30, 33, and 38 GPa], and c [at 16, 19, 21, 24, and 36 GPa] are indicative of relaxation effects to reach the local minimum among all the six degrees of freedom of the lattice. There is no reason to postulate structural phase transitions based solely on these fluctuations,¹⁴ particularly in absence of any discontinuities or “cusps” in the calculated P - V isotherm curve.

The effect of pressure on the HOMO-LUMO gap is displayed in Figure 7a. First we note the decrease of the gap from 1.3 eV at 0 GPa to 0.57 eV at 38 GPa. This notable decrease in the band gap should be discernable experimentally, possibly with enhanced electrical and thermal conductivities, and is indicative of the destabilization of crystal LLM-105 under pressure. With a relatively small initial band gap compared to other energetic materials, initiation mechanisms via electronic excitations accessing the low-lying electronic states could become operative for this material, and even more so under increased pressure.⁴²⁻⁴⁶ Second, similar to the effect of pressure on the lattice parameters noted above, there are several regions in Figure 7 where the HOMO-LUMO gap decrease

is not monotonic, but experiences abrupt change as a function of pressure. This is most notable at 21 GPa where the change is ~ 0.07 eV. The pressure dependence of HOMO and LUMO energies are plotted in Figure 7b, which shows that both orbitals are monotonically increasing with pressure. At pressures of 20 and 21 GPa, the slope of the HOMO is more than double that of the LUMO (0.125 vs 0.06, respectively), and vanishes at 22 GPa. The behavior in the band gap is thus due to changes associated with the HOMO alone, which is located on the oxide N-O. Examining the crystal structures at these points, including calculations of atom-pair distance matrix, did not reveal significant changes other than slight off-plane rotations of the functional groups ($-\text{NO}_2$). We note that all cell parameters have experienced small changes in this region (19 - 22 GPa), so that this change in the HOMO-LUMO gap is a reflection of adjusting to local structural changes. We conjecture that it is at best a high-order, displacive phase transition.

LLM-105's high density of 1.919 g/cm³ is attributed to an extensive system of intra- and intermolecular hydrogen bonds, similar to TATB.² Every hydrogen atom within the lattice is involved in intramolecular hydrogen-bonding to its neighboring oxygen atom, and participates in intermolecular interactions with adjoining molecules. There are two types of intermolecular hydrogen interactions: one involving the oxygen of the N-O, and the other involving that of the NO_2 moieties, as shown in Figure 8. Our two-body dispersion-corrected calculations permit us to examine the behavior of these two interactions under pressure to reveal any possible tendency towards possible bond symmeterization or polymerization⁴⁷ and/or hydrogen bond-equivalency.⁴⁸ The calculated pressure dependence of the intermolecular hydrogen bond lengths is displayed

in Figure 9. These intermolecular hydrogen bonds of the type shown in Figure 8 lie approximately along the *a* (for the N-O---H) and the *c* (for the NO₂---H) lattice directions. The intermolecular bond between the hydrogen of the amino and oxygen of the oxide (N-O) group undergoes a monotonic decrease from about 1.93 Å at the equilibrium geometry to 1.49 Å at P=45 GPa, a change of 0.44 Å. For the same pressure range, the intermolecular amino and oxygen of the dioxide (-NO₂) group undergoes a change from 2.21 Å to 1.72 Å, a change of 0.49 Å. These results indicate that intermolecular compressibility along these directions is near equivalent. It should be noted that at P=45 GPa, the intermolecular bond lengths 1.45 and 1.72 Å are much shorter than a non-covalent N-O...H bond distance. The average intermolecular NO...H bond distance for various nitro-containing compounds was determined to be about 2.3 Å.⁴⁹ Since both of these intermolecular bonds involve interactions with the amine group, it is to be expected that the mid-IR (~3000 cm⁻¹) spectral region of the NH₂ symmetric and antisymmetric stretches would exhibit strong perturbations from increased contributions of these types of interactions.

Finally, structural changes within the pressure range of the current calculations are confined to slight torsional angles of the NO₂ groups. We do not observe any tendency towards pressure-induced chemical transformations, or any tendency towards dimerization or polymerization. The aromaticity of molecular LLM-105 and the strong intermolecular interactions could explain its relative thermal stability.

C. Heat of Formation.

The heat of formation of solid LLM-105 at room temperature can be obtained via Hess's law as the difference between the heat of formation of the gas-phase and the heat of sublimation:

$$\Delta H_{f(s)}^0 = \Delta H_{f(g)}^0 - \Delta H_{sub}$$

To our knowledge, there are no reported experimental measurements of any of these quantities. We calculated $\Delta H_{f(g)}^0$ using the Gaussian-4 theory (G4 theory), which has been shown to provide average deviation from experimental determinations of ~ 1 kcal/mol for a test set containing 454 data,³⁰ and with the CCCA-PS3 method. We calculate an approximate value for ΔH_{sub} as the difference between the electronic energy of the crystal (for the 3x1x2 supercell) and of the gas (one molecule in a cubic box with a dimension of 30 Å) and adding the appropriate thermal correction.

The theoretical gas phase heat of formation for LLM-105, $\Delta H_{f(g)}^0$, with composition $C_4H_4N_6O_5$ can be calculated at $T=298$ as follows:⁵⁰

$$\begin{aligned} \Delta H_f^0(C_4H_4N_6O_5, 298 \text{ K}) \\ &= \Delta H_f^0(C_4H_4N_6O_5, 0 \text{ K}) \\ &+ [H^0(C_4H_4N_6O_5, 298 \text{ K}) - H^0(C_4H_4N_6O_5, 0 \text{ K})] \\ &- 4[H^0(C, 298 \text{ K}) - H^0(C, 0 \text{ K})]_{ST} - 4[H^0(H, 298 \text{ K}) - H^0(H, 0 \text{ K})]_{ST} \\ &- 6[H^0(N, 298 \text{ K}) - H^0(N, 0 \text{ K})]_{ST} - 5[H^0(O, 298 \text{ K}) - H^0(O, 0 \text{ K})]_{ST} \end{aligned}$$

The enthalpy of formation at 0 K is given by:

$$\begin{aligned}
& \Delta H_f^0(\text{C}_4\text{H}_4\text{N}_6\text{O}_5, 0 \text{ K}) \\
&= 4\Delta H_f^0(\text{C}, 0 \text{ K}) + 4\Delta H_f^0(\text{H}, 0 \text{ K}) + 6\Delta H_f^0(\text{N}, 0 \text{ K}) + 5\Delta H_f^0(\text{O}, 0 \text{ K}) \\
&\quad - \sum D_0
\end{aligned}$$

The JANAF values for the atomic ΔH_f^0 and for the standard state of the elements, $[H^0(298 \text{ K}) - H^0(0 \text{ K})]_{ST}$, are used in the above equations.⁵¹ The nonrelativistic atomization energies, $\sum D_0$, and enthalpies $H^0(\text{C}_4\text{H}_4\text{N}_6\text{O}_5)$ at 298 and 0 K determined from the G4 theory are: $\sum D_0 = 1826.08 \text{ kcal/mol}$, $[H^0(\text{C}_4\text{H}_4\text{N}_6\text{O}_5, 298 \text{ K}) - H^0(\text{C}_4\text{H}_4\text{N}_6\text{O}_5, 0 \text{ K})] = 8.47 \text{ kcal/mol}$. The gas phase heat of formation of LLM-105 at 0 and 298 K are then: $\Delta H_f^0(\text{C}_4\text{H}_4\text{N}_6\text{O}_5, 0 \text{ K}) = 30.49 \text{ kcal/mol}$, and $\Delta H_f^0(\text{C}_4\text{H}_4\text{N}_6\text{O}_5, 298 \text{ K}) = 22.48 \text{ kcal/mol}$. The CCCA-PS3 method uses larger basis sets than the G4 method without empirical parameters, but achieves a similar level of overall accuracy. For the CCCA-PS3 method, we find $\Delta H_f^0(\text{C}_4\text{H}_4\text{N}_6\text{O}_5, 298 \text{ K}) = 25.92 \text{ kcal/mol}$. The difference between the G4 and CCCA-PS3 values reflects the difficulties in accurately calculating heats of formation for large molecules.

The heat of sublimation can be calculated from the approximation:⁵²⁻⁵⁴

$$\Delta H_{sub}(T) = -E_{lat} - 2RT,$$

where the lattice energy E_{lat} is given as:

$$E_{lat} = \frac{E_S}{Z} - E_g.$$

E_S is the total energy of a unit cell, Z is the number of molecules per unit cell, and E_g is the total energy of the molecule in the gas phase at its lowest energy conformation. It

should be noted that the above expression for ΔH_{sub} assumes several approximations such as the intramolecular frequencies of the crystal and the gas phase are the same, the temperature is high enough so that the contribution of the intermolecular vibrations is $6RT$, and intermolecular zero-point effects are negligible.⁵³ Thus, our evaluation of ΔH_{sub} reduces to calculating the terms of E_{lat} at the same level of theory.

From the optimized geometry of the 3x1x2 supercell, we find $\frac{E_S}{Z} = -164.774924$ Hartree. From the optimization of one LLM-105 molecule in a cell volume of $27 \times 10^3 \text{ \AA}^3$ at the same level of theory, $E_g = -164.721393$ Hartree. From these results, we find $E_{lat} = -33.6$ kcal/mol, and $\Delta H_{sub}(298.15 \text{ K}) = 32.4$ kcal/mol. From Hess's law, we estimate the heat of formation of solid LLM-105 at $T=298.15 \text{ K}$ to be $\Delta H_{f(s)}^0 = -9.9$ kcal/mol or -6.5 kcal/mol, using the calculated $\Delta H_{f(g)}^0$ values from G4 and CCCA-PS3, respectively.

IV. Conclusion

We performed dispersion-corrected DFT calculations on the equilibrium crystal structure and hydrostatic compression of LLM-105 up to pressure of 45 GPa. We determined that adequate k-points sampling in the Brillouin zone is required to reproduce the experimental X-ray lattice parameters of the equilibrium structure. Convergence tests showed that a 3x1x2 k-point mesh or greater is necessary to achieve good results. Our supercell model calculations of 3x1x2 dimension for the zero temperature P-V isotherm EOS provided a bulk pressure modulus $B_0 = 19.18 \pm 0.2$ GPa and its derivative $B'_0 = 7.22 \pm 0.1$ for the entire pressure range. The compressibility of LLM-105 is anisotropic, more enhanced along the b lattice vector. The calculated HOMO-LUMO energy gap showed a decrease from 1.3 eV at 0 GPa to 0.6 eV at 45 GPa. This

significant reduction could play a role in the initiation mechanism via electronic state excitation for this material, and invite further experimental investigations to confirm or exclude the semiconductor like behavior of this organic molecular solid. Our calculations showed that the intermolecular $\text{-NO}_2\text{—H}_2\text{N-}$ and $\text{-NO—H}_2\text{N-}$ hydrogen bonds decrease significantly upon compression, which should be discernible by IR spectroscopic signatures. Small cell parameters, structural fluctuations with pressure, amide symmetry breaking, do not point to structural transitions, polymerization or chemical transformations within the pressure regime of this study. We calculated the gas phase and the condensed phase heat of formation at $T=298\text{ K}$.

Acknowledgments:

This work is performed under the auspices of the U.S. Department of Energy Lawrence Livermore National Laboratory under Contract DE-AC52-07NA27344. Support from the Advanced Scientific Computation (ASC) program and computational resources via the Computational Grand Challenge Program are greatly appreciated.

Figure Captions:

Figure 1. (a) Molecular LLM-105.

(b) The unit cell crystal structure.

Figure 2. Total and partial (s and p) electronic density of states (DOS) of LLM-105 at 0.0 GPa.

Figure 3. Temporal profiles of pressure (diagonal components), temperature, and volume from the NPT molecular dynamics simulation.

Figure 4. P-V hydrostatic isotherm of LLM-105 as determined in (a) up the experimental results of ~ 6 GPa from Ref. ⁸ and from this work, and (b) this work up to 45 GPa. The solid line in (b) is the fit to the Birch-Murnaghan EOS.

Figure 5. Calculated and experimental pressure dependence of LLM-105 lattice parameters. (a) a , (b) b , and (c) c .

Figure 6. Pressure dependence of lattice angles (a) α and γ relative to 90° , and (b) β .

Figure 7. Calculated pressure dependence of (a) the HUMO-LUMO energy gap, (b) HOMO and LUMO.

Figure 8. Intermolecular hydrogen bonds in LLM-105 involving the oxide N-O and dioxide NO_2 moieties.

Figure 9. Calculated pressure dependence of intermolecular hydrogen bond lengths.

Table I. Lattice parameters of LLM-105 crystal.

	a (Å)	b (Å)	c (Å)	α (°)	β (°)	γ (°)	V (Å ³)
<u>k-point:</u>							
2x1x2	5.781	15.631	8.498	90.00	101.42	90.00	752.65
3x1x2	5.701	15.721	8.435	90.00	100.65	90.00	743.06
6x2x4	5.701	15.718	8.436	90.00	100.65	90.00	742.92
<u>Supercell:</u>							
1x1x1	4.042	19.586	8.761	89.97	97.61	90.16	687.55
2x1x2	5.771	15.631	8.441	90.00	101.30	90.01	746.71
3x1x2	5.714	15.727	8.414	90.00	100.81	89.99	742.66
6x2x4	5.754	15.604	8.477	90.00	101.22	90.00	746.55
<u>Experiment:</u> ^a							
	5.716	15.850	8.414	90.00	101.04	90.00	748.16
<u>PCW:</u> ^b							
LDA	5.837	15.579	8.221		99.51		737.24
GGA/PW91	6.008	18.279	8.706		100.75		939.23

^a From Ref. ²

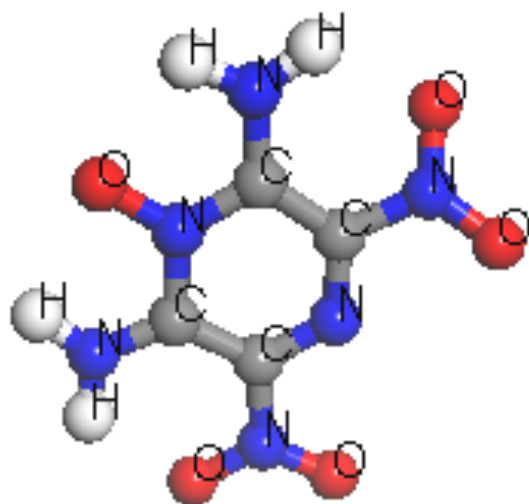
^b. Previous computational work from Ref. ¹⁴

Table II. Comparison of bulk pressure modulus (B_0) and its pressure derivative (B'_0) from 3rd order Birch-Murnaghan EOS fits.

Parameter	This work ^a	Experiment ^b
$B_0(GPa)$	17.37 ± 1.44 (19.18 ± 0.2)	11.19
B'_0	7.89 ± 1.34 (7.22 ± 0.1)	18.54

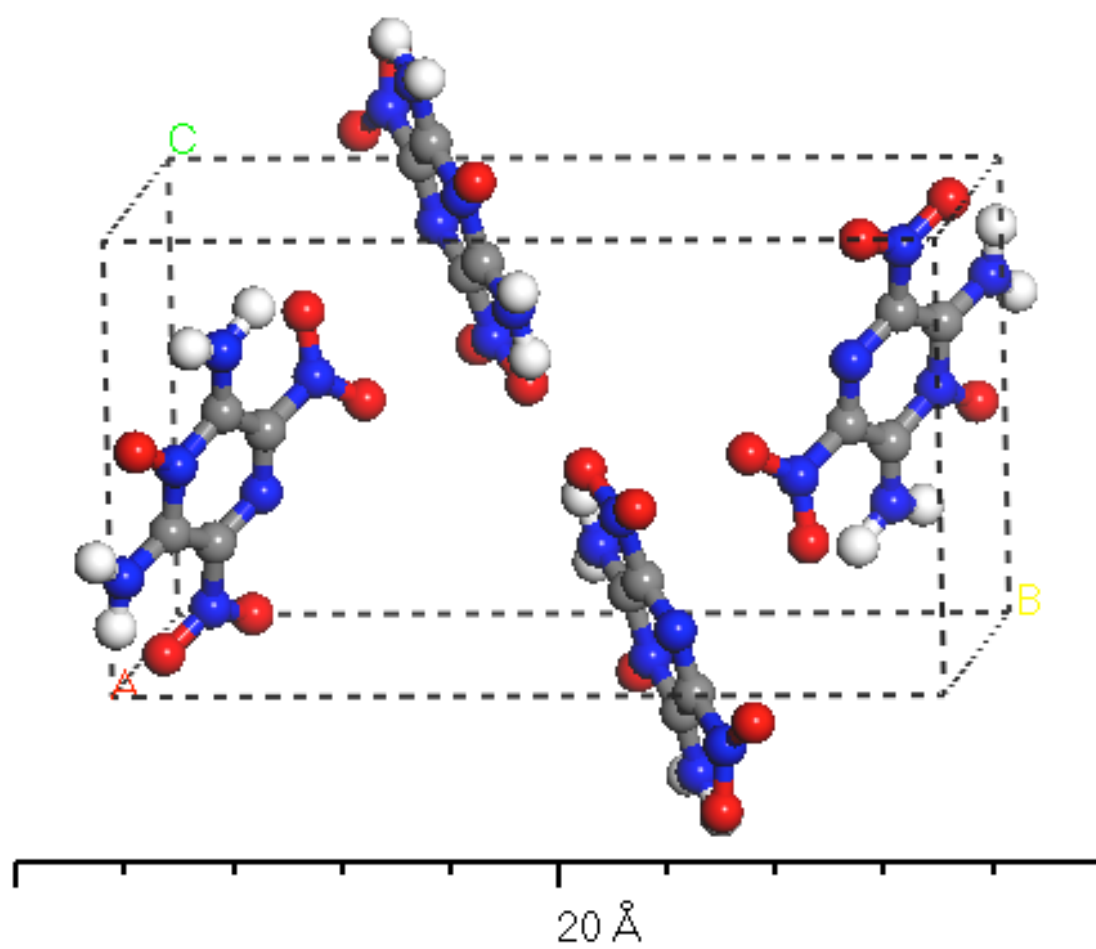
^a This work; P-V fit using pressures up to 6 GPa . A fit using pressures of up to 45 GPa is in parenthesis.

^b Experimental results at ambient temperature from Ref. ⁸



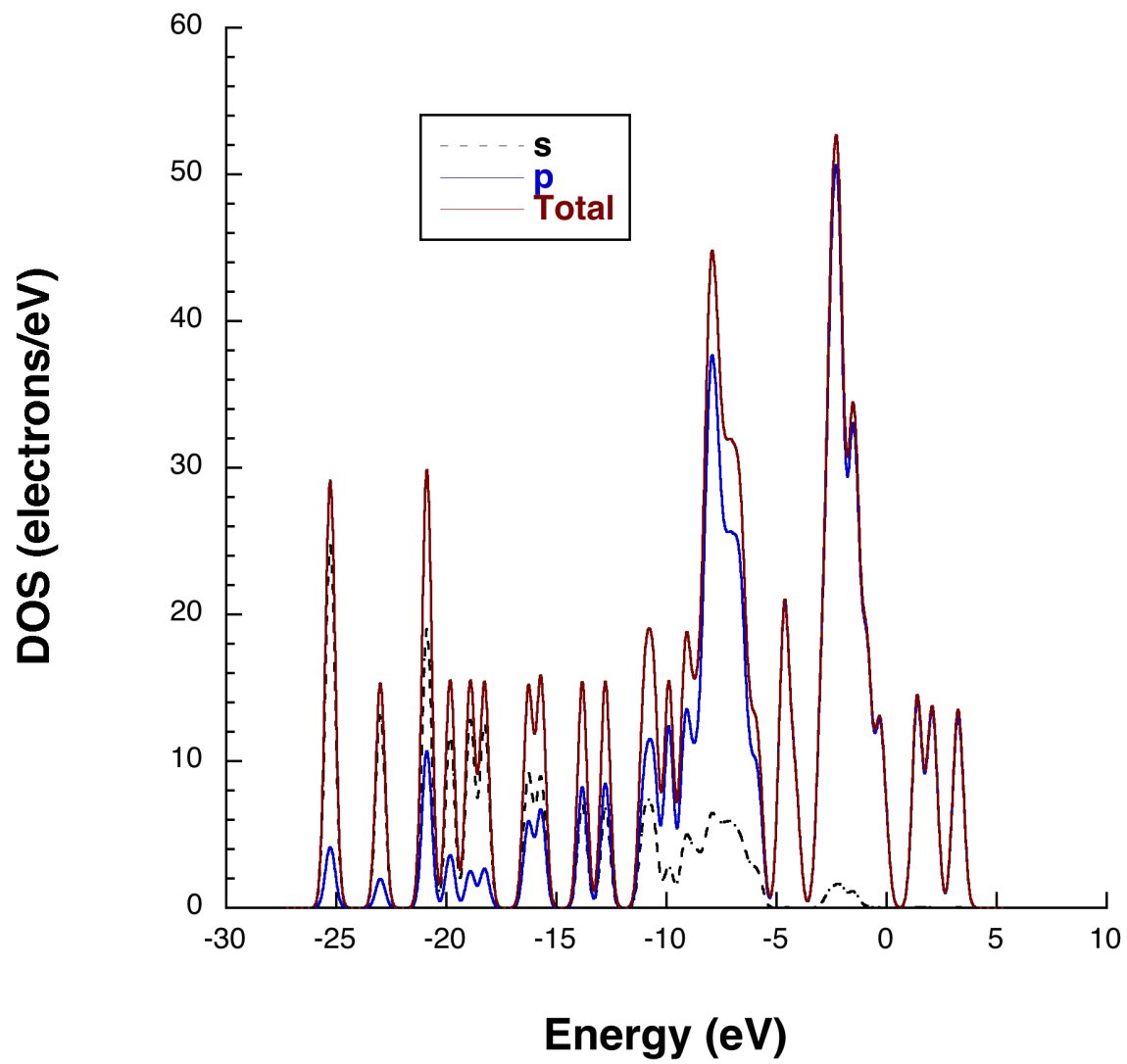
(a)

Manaa et al.: Figure 1a.

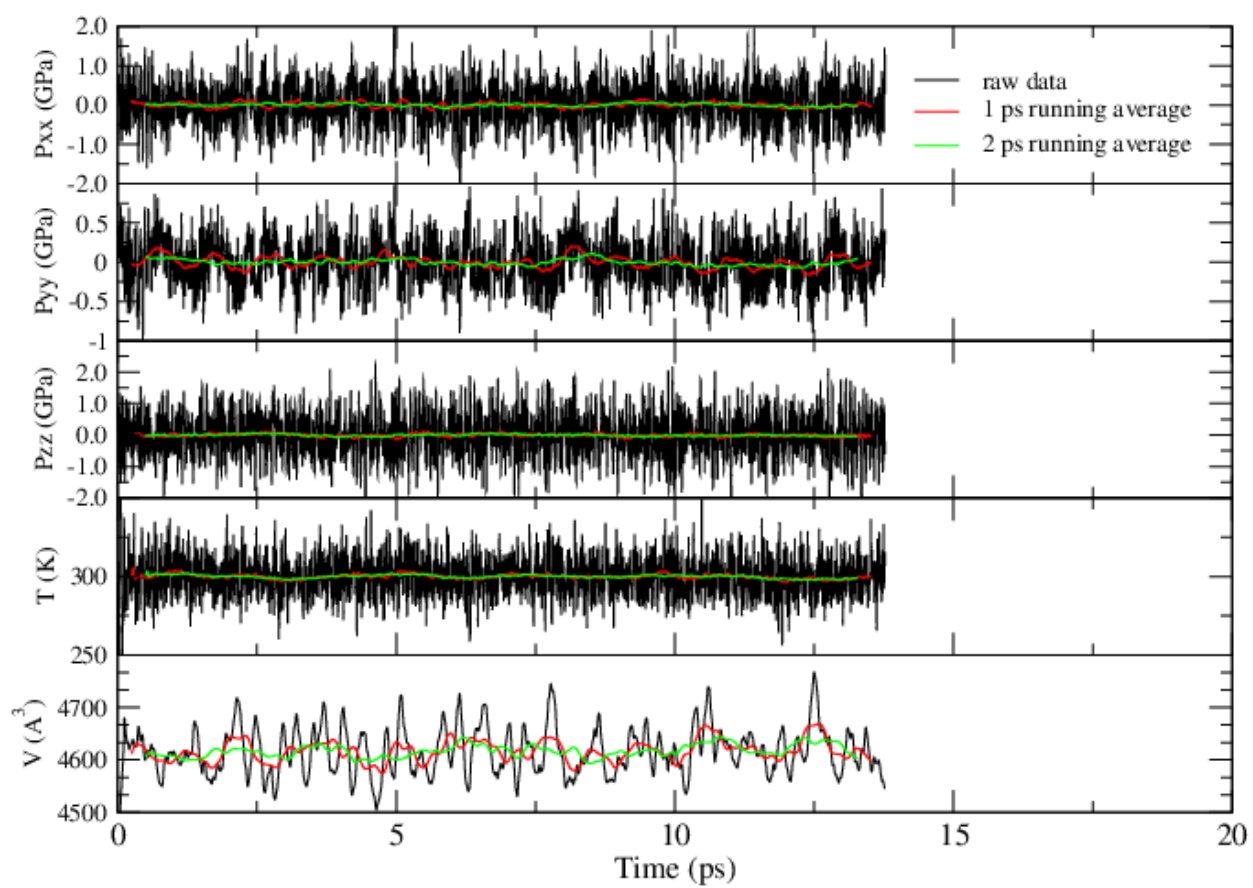


(b)

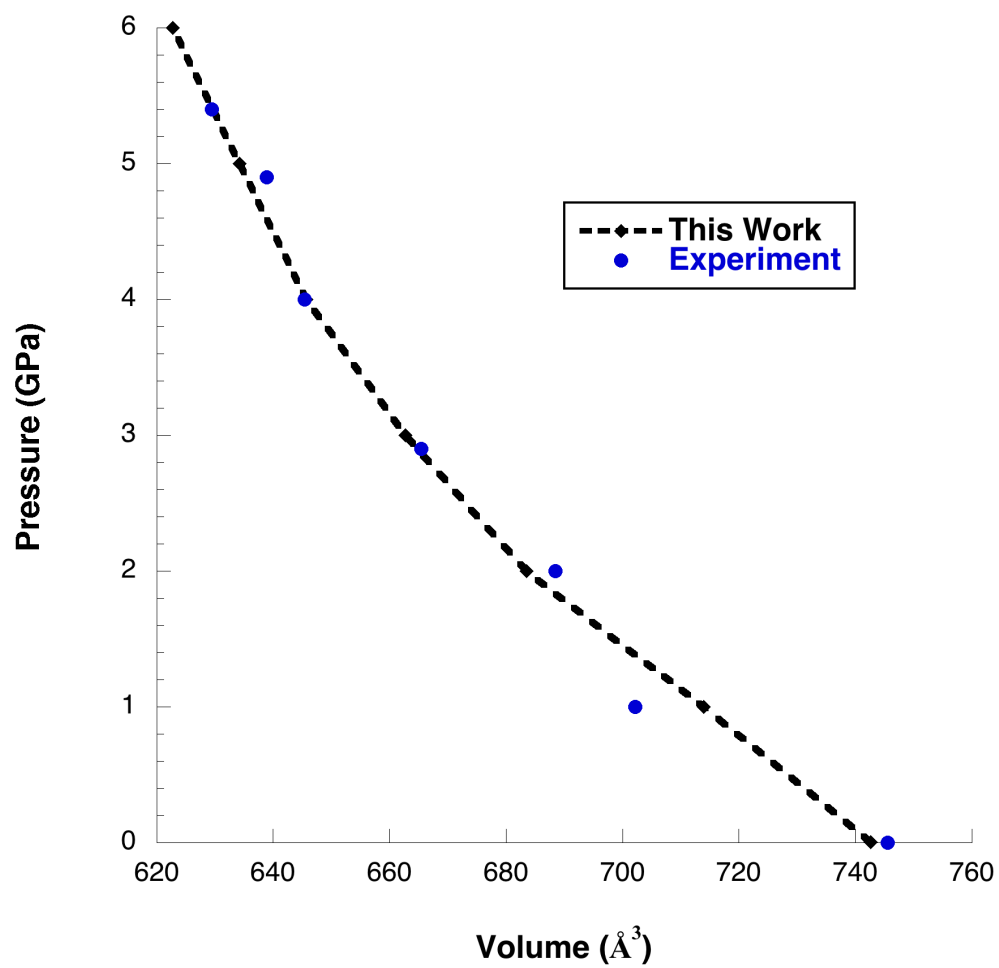
Manaa et al.: Figure 1b.



Manaa et al.: Figure 2.

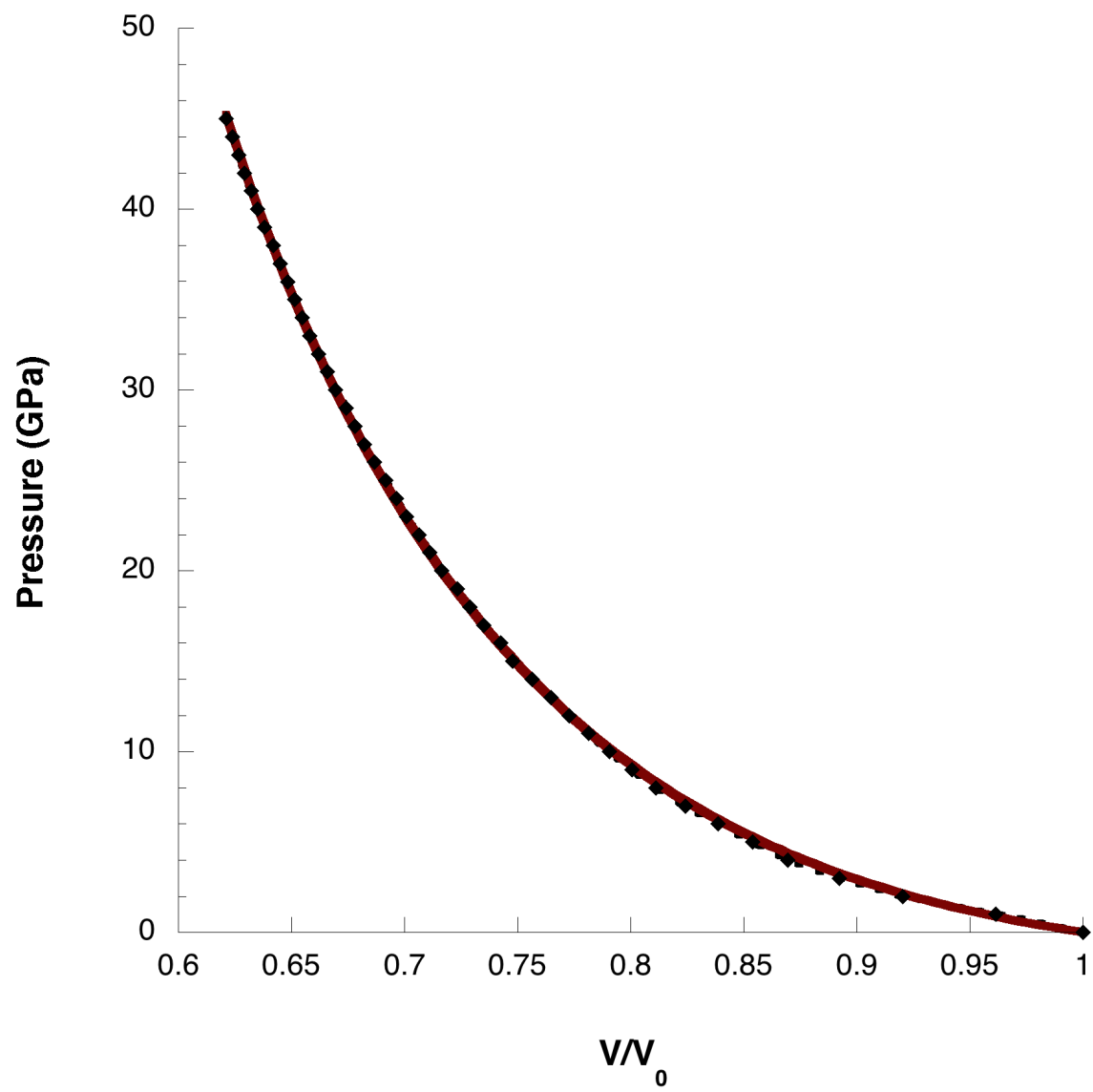


Manaa et al.: Figure 3.



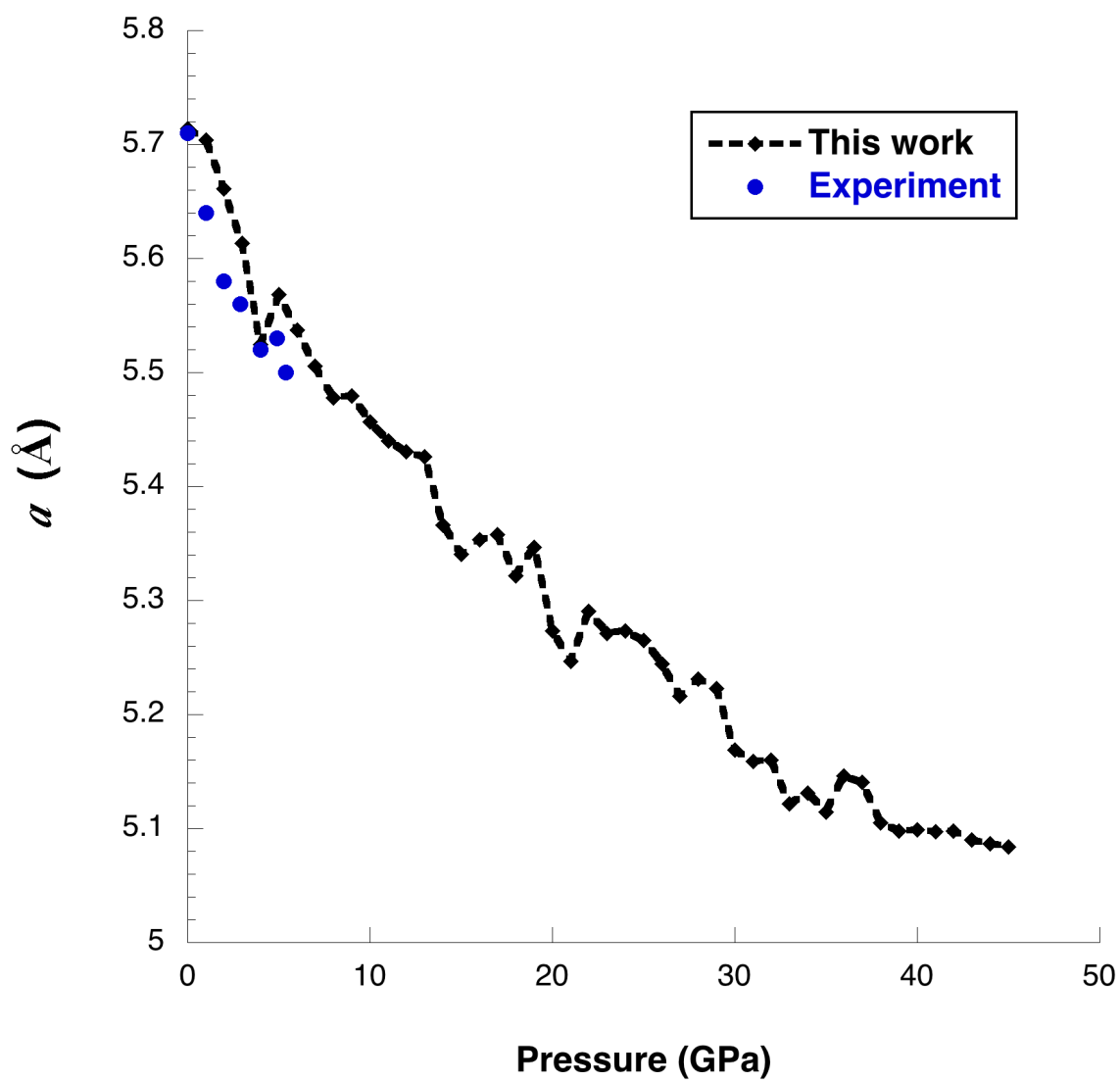
(a)

Manaa et al.: Figure 4a.



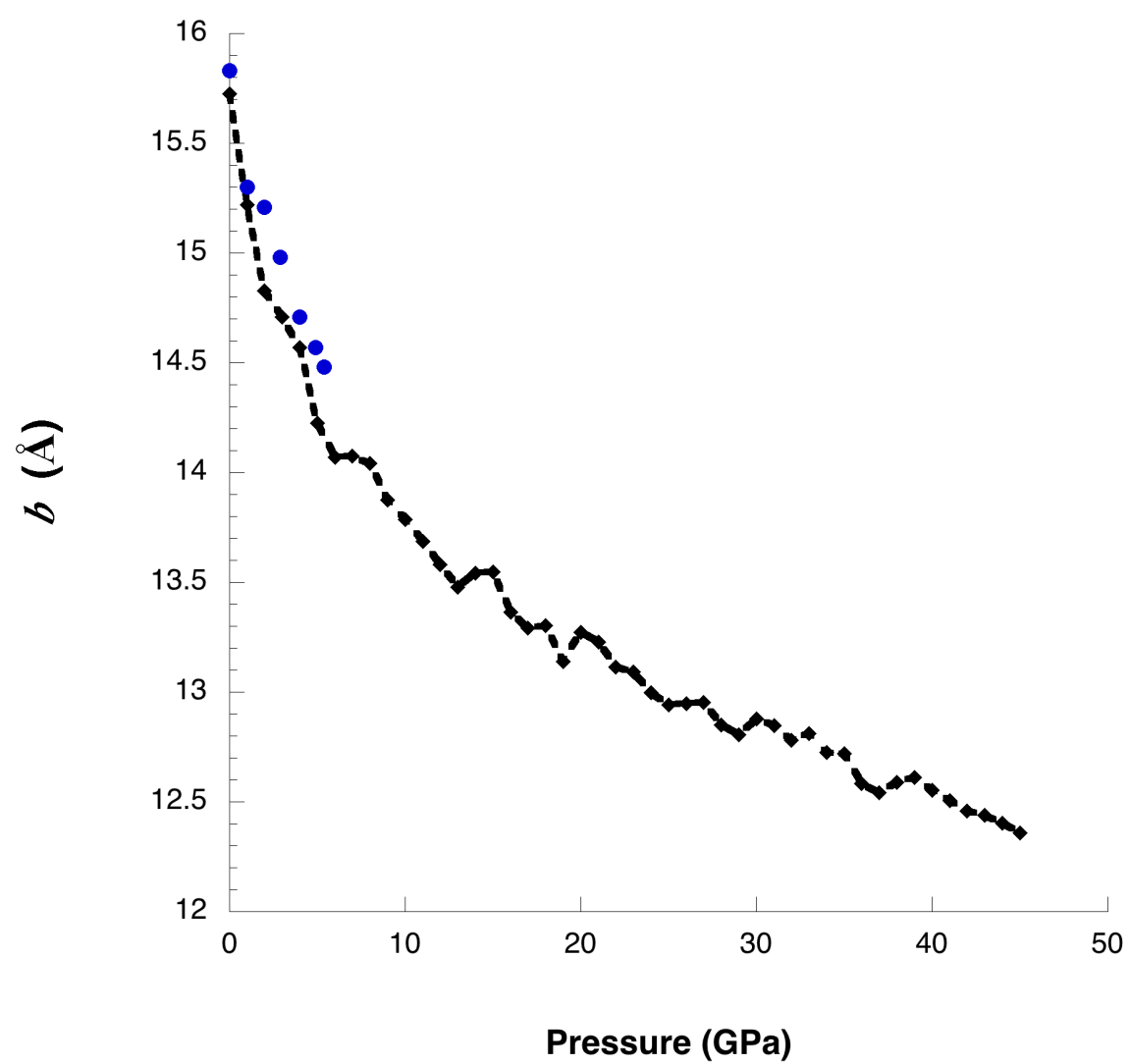
(b)

Manaa et al.: Figure 4b.



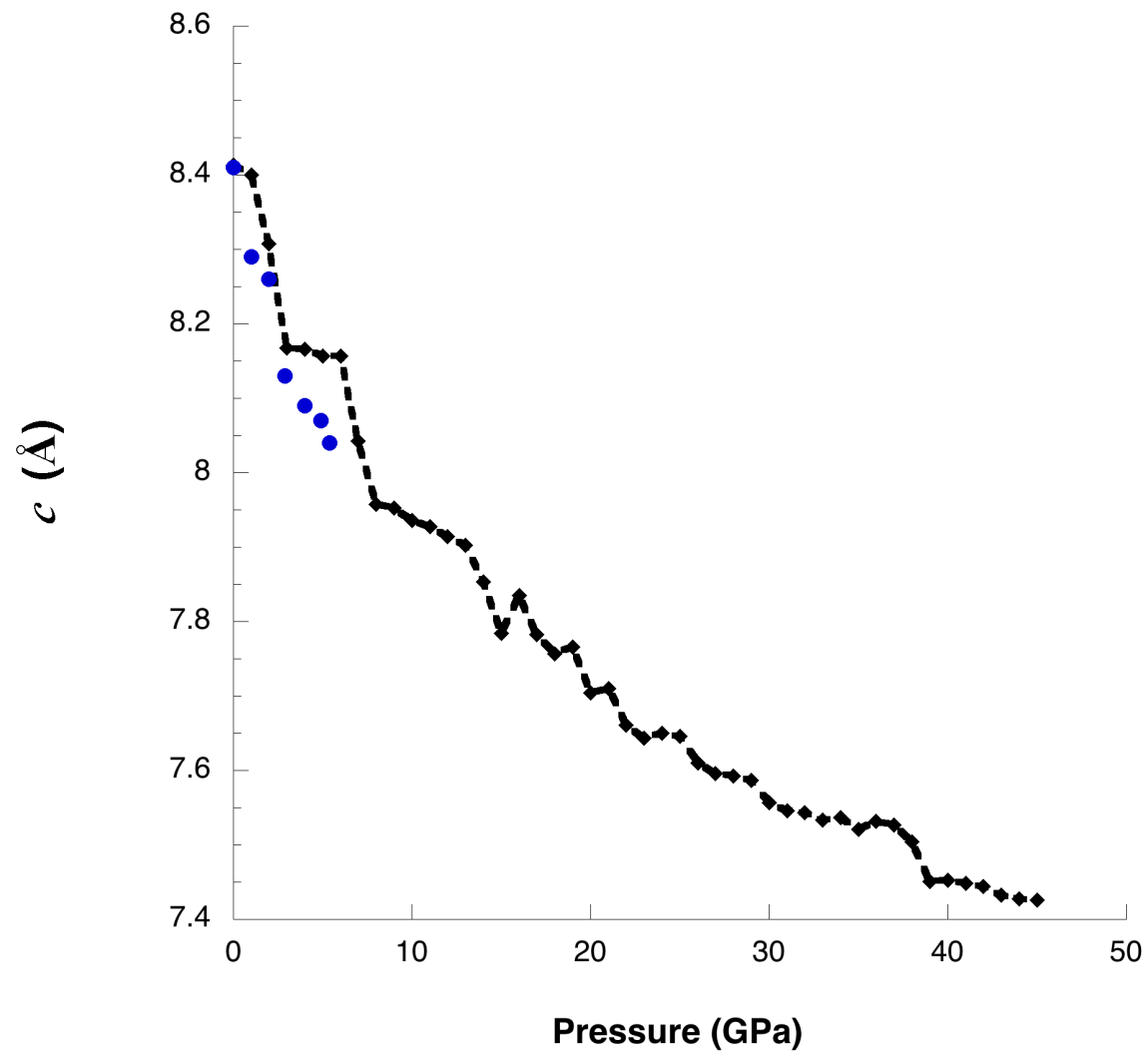
(a)

Manaa et al.: Figure 5a.



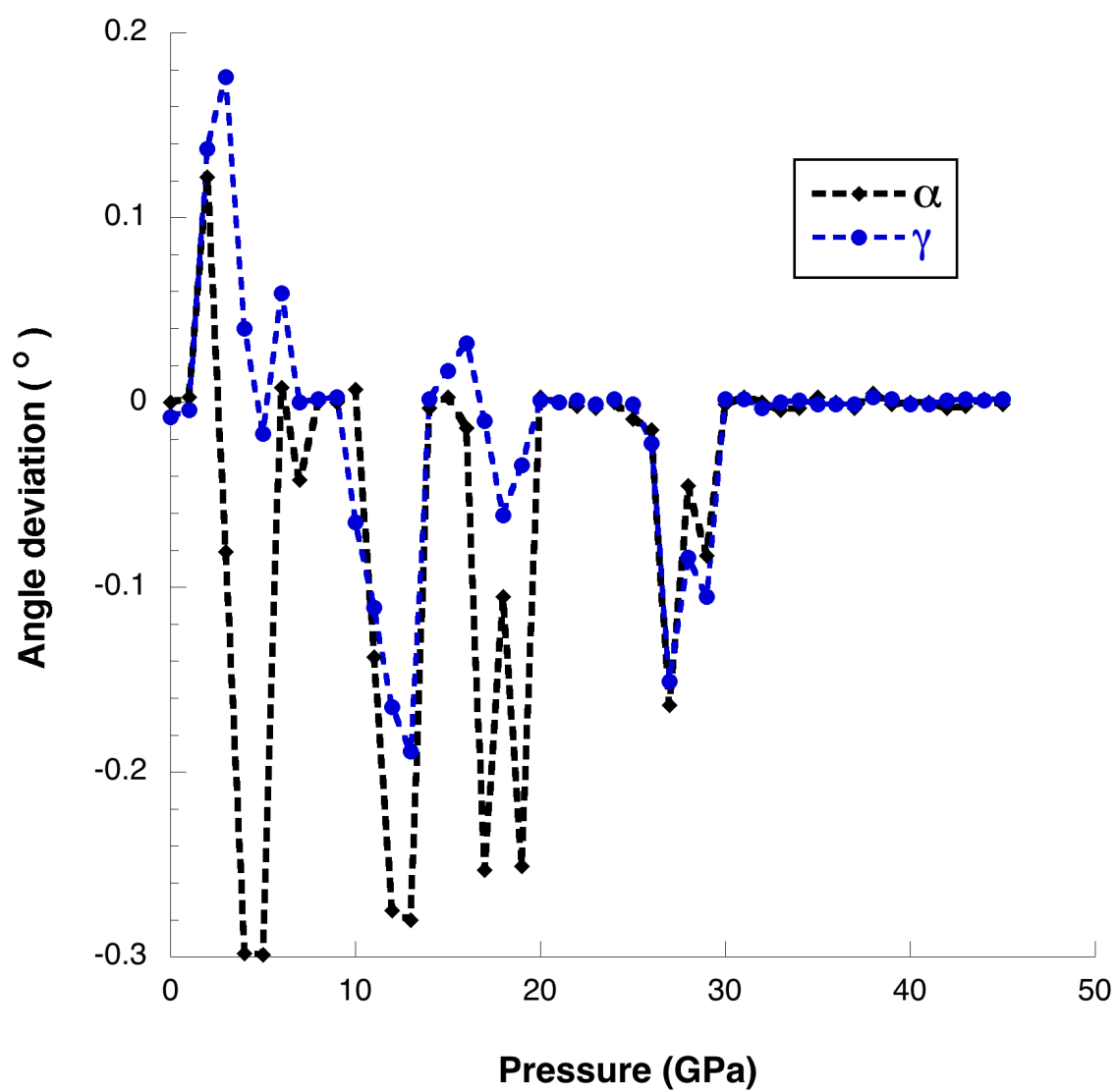
(b)

Manaa et al.: Figure 5b.



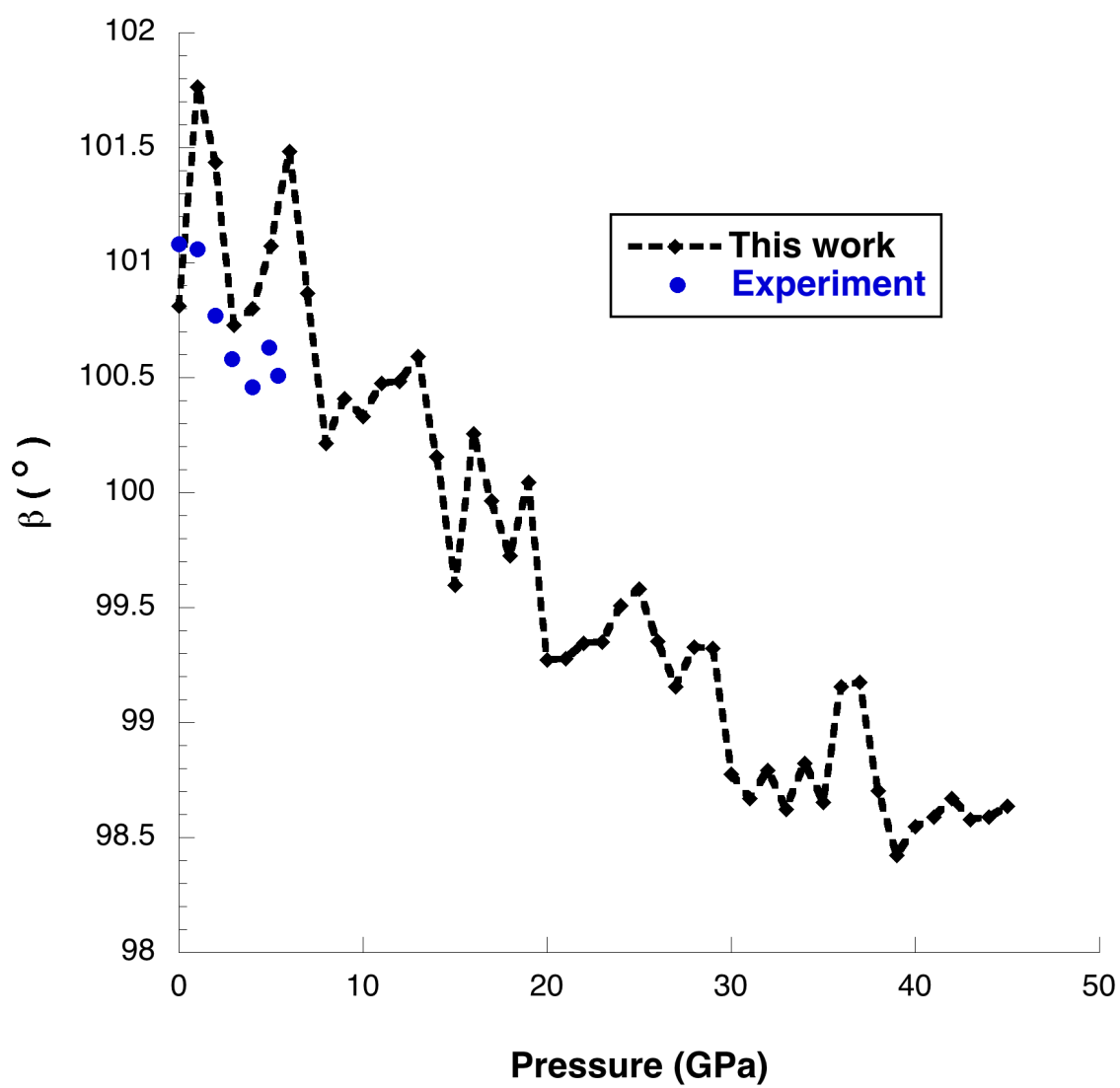
(c)

Manaa et al.: Figure 5c.



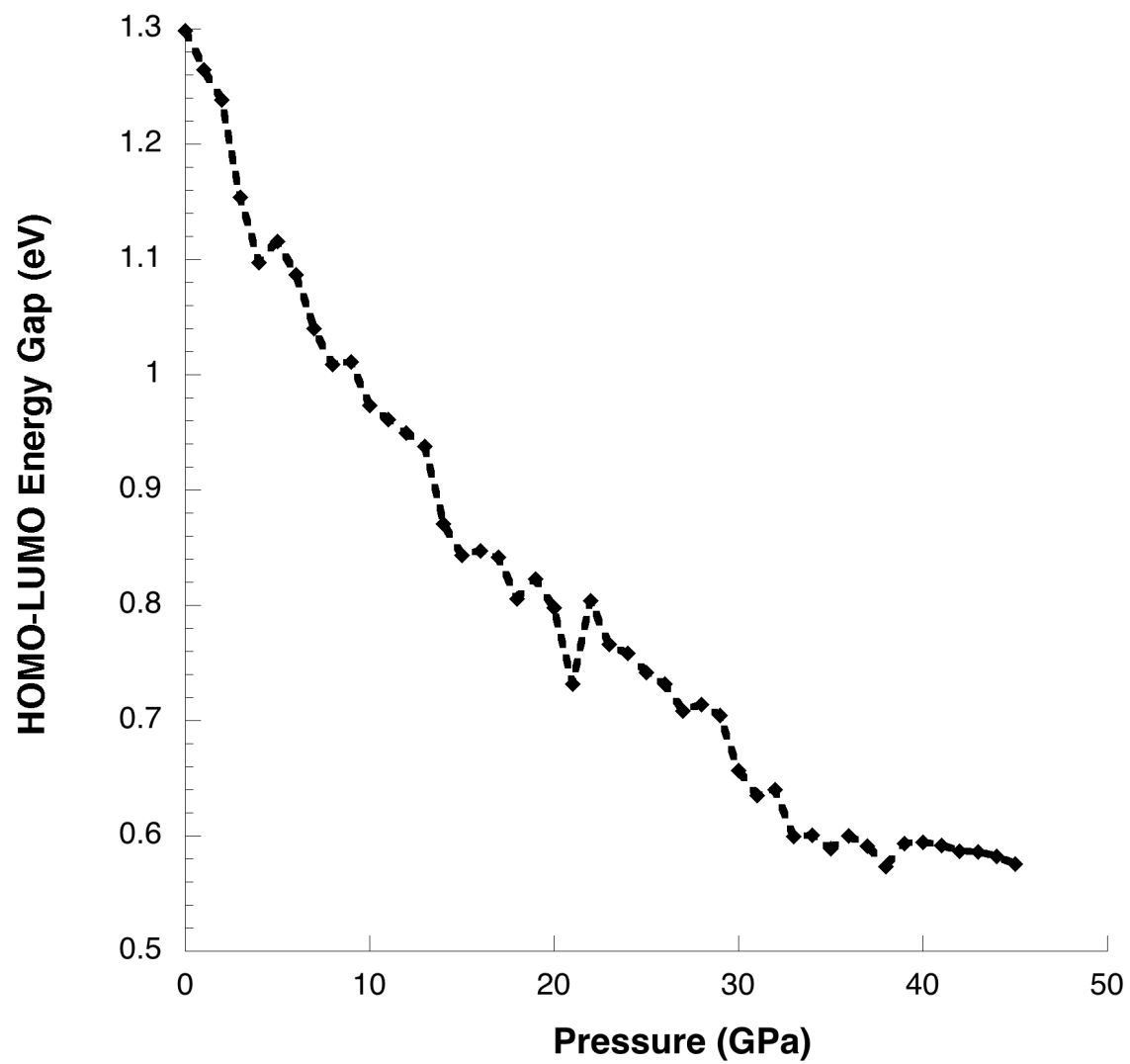
(a)

Manaa et al.: Figure 6a.



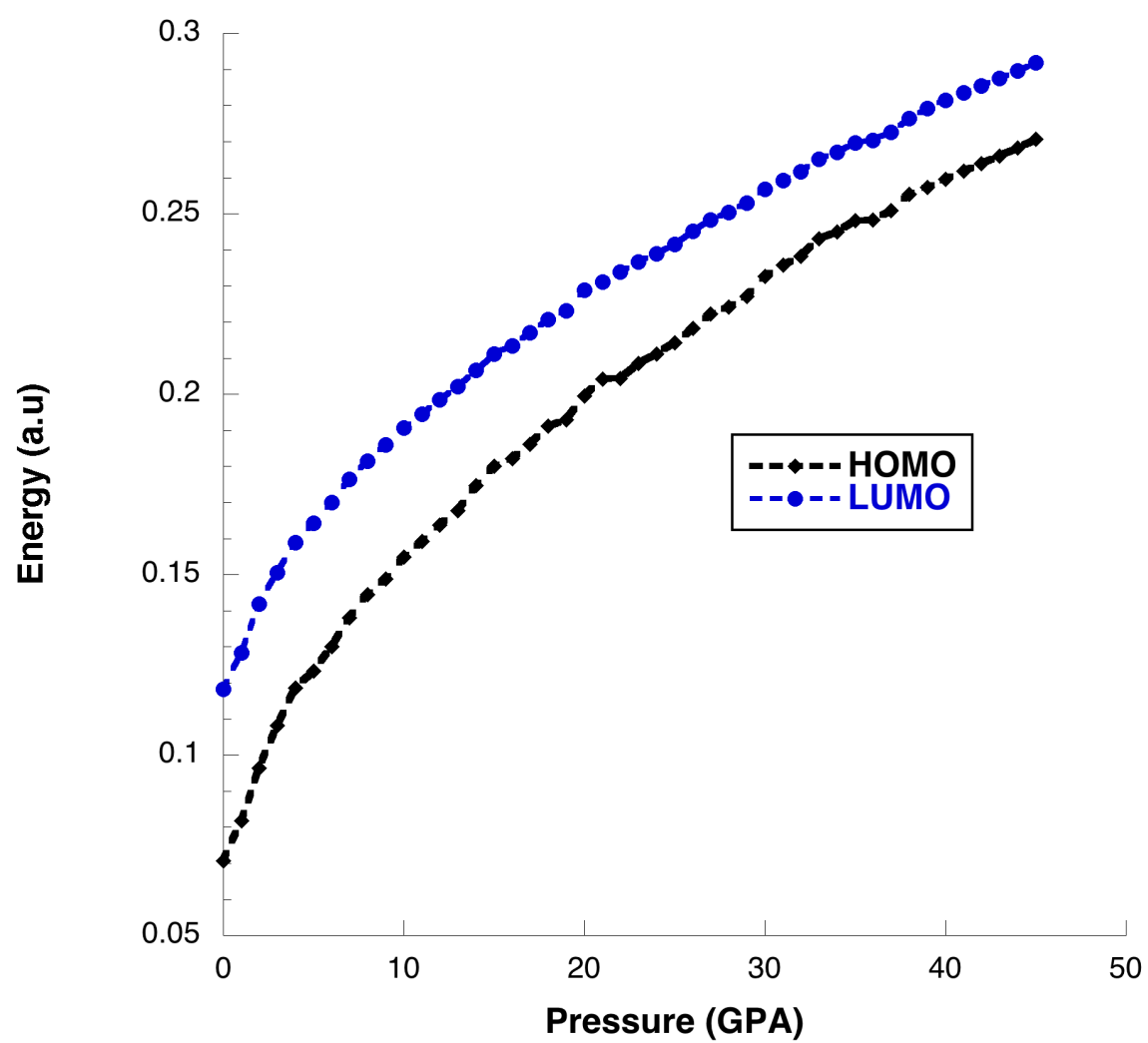
(b)

Manaa et al.: Figure 6b.



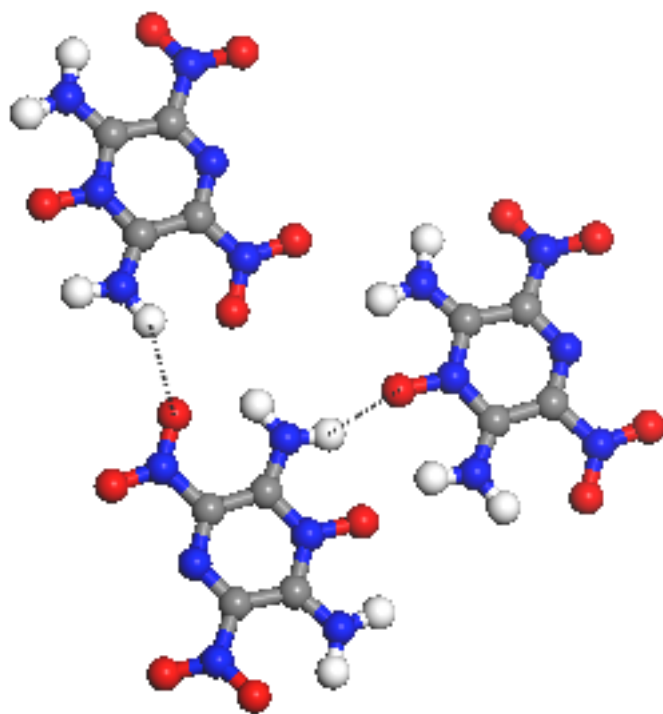
(a)

Manaa et al.: Figure 7a.

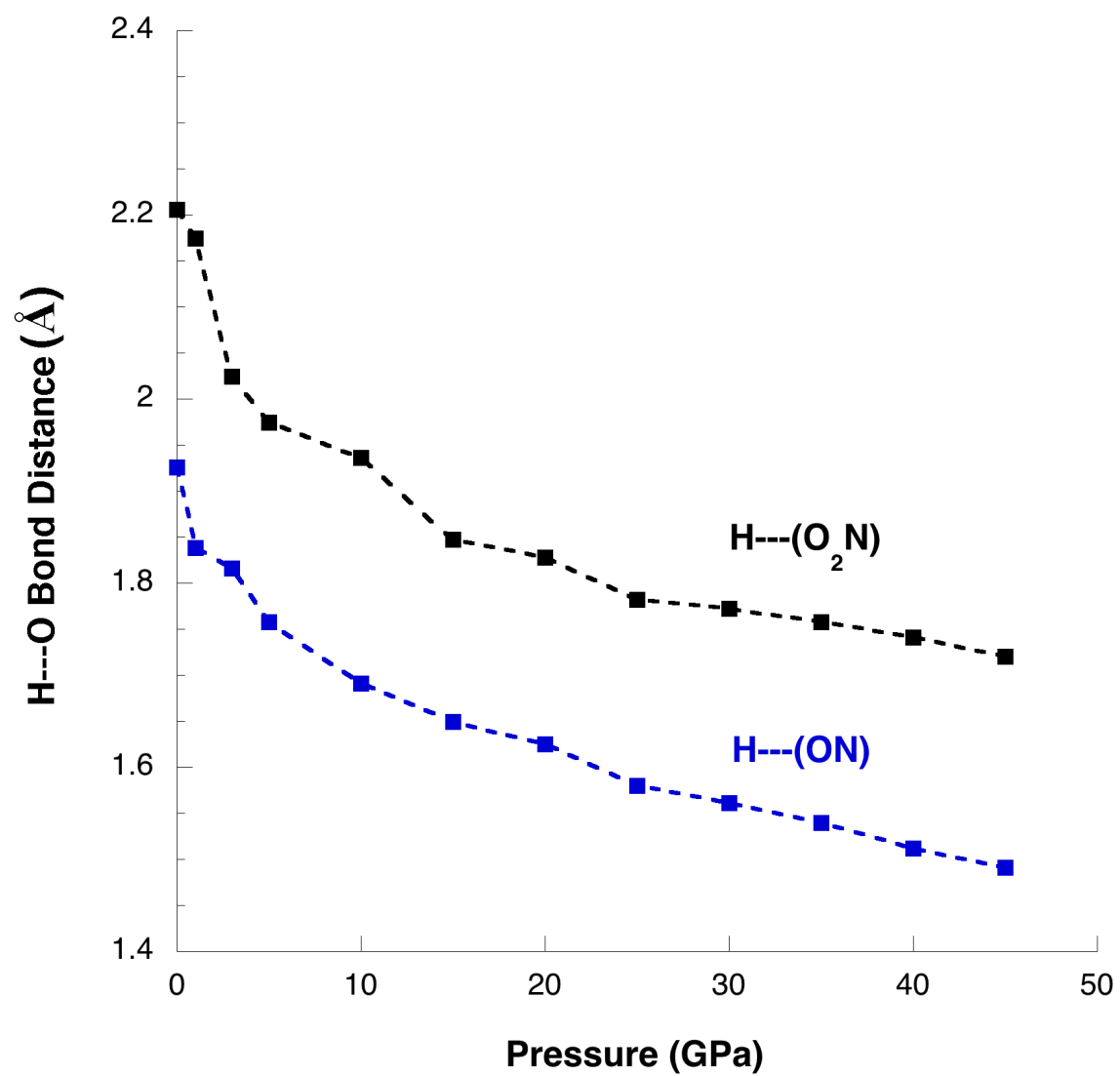


(b)

Manaa et al.: Figure 7b.



Manaa et al.: Figure 8.



Manaa et al.: Figure 9.

References:

1. P. F. Pagoria, A. R. Mitchell, R. D. Schmidt, R. Simpson, F. Garcia, J. W. Forbes, R. Swansiger and D. Hoffman, Report No. UCRL-JC-130518, (1998).
2. R. D. Gilardi and R. J. Butcher, *Acta Cryst.* **E57**, o657-o658 (2001).
3. J. R. Kolb and H. F. Rizzo, *Propellants Explos.* **4**, 10 (1979).
4. M. R. Manaa and L. E. Fried, *J. Phys. Chem. A* **105**, 6765 (2001).
5. C. M. Tarver, P. A. Urtiew and T. D. Tran, *J. Energ. Mat.* **23**, 183 (2005).
6. T. Tran, P. Pagoria, D. Hoffman, B. Cunningham, R. Simpson, R. Lee and L. Cutting, in *Proceedings of the 12th International Detonation Symposium*, San Diego, CA, (2002).
7. H. X. Ma, J. R. Song, F. Q. Zhao, H. X. Gao and R. Z. Hu, *Chin. J. Chem.* **26** (11), 1997 (2008).
8. J. C. Gump, C. A. Stoltz, B. P. Mason, B. G. Freedman, J. R. Ball and S. M. Peiris, *J. Appl. Phys.* **110** (7) (2011).
9. E. F. C. Byrd and B. M. Rice, *J. Phys. Chem. C* **111**, 2787 (2007).
10. S. Grimme, *J. Comp. Chem.* **27**, 1787 (2006).
11. S. Grimme, J. Antony, S. Ehrlich and H. Krieg, *J. Chem. Phys.* **132**, 154104 (2010).
12. A. Tkatchenko and M. Scheffler, *Phys. Rev. Lett.* **102**, 073005 (2009).
13. H. J. Monkhorst and J. D. Pack, *Phys. Rev. B* **13**, 5188 (1976).
14. Q. Wu, C. Yang, Y. Pan, F. Xiang, Z. Liu, W. Zhu and H. Xiao, *J. Molec. Mod.* **19**, 5159 (2013).
15. H. Liu, J. Zhao, J. Du, Z. Gong, G. Ji and D. Wei, *Phys. Lett. A* **367**, 383 (2007).
16. C. J. Wu, L. H. Yang, L. E. Fried, J. Quenneville and T. J. Martinez, *Phys. Rev. B* **67**, 235101 (2003).
17. W. H. Zhu, X. W. Zhang, T. Wei and H. M. Xiao, *Theo. Chem. Acc.* **124**, 179 (2009).
18. J. P. Perdew, K. Burke and M. Ernzerhof, *Phys. Rev. Lett.* **78**, 1396 (1997).
19. D. Vanderbilt, *Phys. Rev. B* **41**, 7892 (1990).
20. G. Kresse and J. Furthmuller, *Phys. Rev. B* **54**, 11169 (1996).
21. B. G. Pfrommer, M. Cote, S. G. Louie and M. L. Cohen, *J. Com. Phys.* **131**, 233 (1997).
22. S. J. Clark, M. D. Segall, C. J. Pickard, P. J. Hasnip, M. J. Probert, K. Refson and M. C. Payne, *Zeits. Fur Kristall.* **220**, 567 (2005).
23. S. Goedecker, M. Teter and J. Hutter, *Phys. Rev. B* **54**, 1703 (1996).
24. J. Schmidt, J. VandeVondele, I. F. W. Kuo, D. Sebastiani, J. I. Siepmann, J. Hutter and C. J. Mundy, *J. Phys. Chem. B* **113** (35), 11959 (2009).
25. J. VandeVondele and J. Hutter, *J. Chem. Phys.* **118**, 4365 (2003).
26. G. J. Martyna, M. E. Tuckerman, D. J. Tobias and M. L. Klein, *Molec. Phys.* **87**, 1117 (1996).
27. S. Nose, *J. Chem. Phys.* **81**, 511 (1984).
28. G. Lippert, J. Hutter and M. Parrinello, *Molec. Phys.* **92**, 477 (1997).

29. J. VandeVondele, M. Krack, F. Mohamed, M. Parrinello, T. Chassaing and J. Hutter, *Comp. Phys. Comm.* **167**, 103 (2005).
30. L. A. Curtiss, P. C. Redfern and K. Raghavachari, *J. Chem. Phys.* **126**, 084108 (2007).
31. M. J. Frisch et al., *Gaussian 09*, Rev.B01 (Gaussian, Inc., Wallingford CT, 2010).
32. K. R. Jorgensen, G. A. Oyedepo and A. K. Wilson, *J. Haz. Mat.* **186**, 583 (2011).
33. N. J. DeYonker, T. R. Cundari and A. K. Wilson, *J. Chem. Phys.* **124**, 114104 (2006).
34. M. W. Schmidt, K. K. Baldridge, J. A. Boatz, S. T. Elbert, M. S. Gordon, J. H. Jensen, S. Koseki, N. Matsunaga, K. A. Nguyen, S. J. Su, T. L. Windus, M. Dupuis and J. A. Montgomery, *J. Comp. Chem.* **14**, 1347 (1993).
35. L. A. Curtiss, K. Raghavachari, P. C. Redfern, V. Rassolov and J. A. Pople, *J. Chem. Phys.* **109**, 7764 (1998).
36. S. F. Sousa, P. A. Fernandes and M. J. Ramos, *J. Phys. Chem. A* **111**, 10439 (2007).
37. C. Hong-Ling, J. Guang-Fu, C. Xiang-Rong, Z. Wei-Hua, Z. Feng, W. Ya and W. Dong-Qing, *J. Phys. Chem. A* **114**, 1082 (2010).
38. M. W. Conroy, Oleynik, II, S. V. Zybin and C. T. White, *J. Appl. Phys.* **104**, 053506 (2008).
39. J. P. Perdew and M. Levy, *Phys. Rev. Lett.* **51**, 1884 (1983).
40. H. Akamatsu and H. Inokuchi, *J. Chem. Phys.* **18**, 810 (1950).
41. F. Birch, *Phys. Rev.* **71**, 809 (1947).
42. A. Bhattacharya, Y. Q. Guo and E. R. Bernstein, *J. Chem. Phys.* **136**, 024321 (2012).
43. M. M. Kuklja, E. V. Stefanovich and A. B. Kunz, *J. Chem. Phys.* **112**, 3417 (2000).
44. M. R. Manaa and L. E. Fried, *J. Phys. Chem. A* **103**, 9349 (1999).
45. B. Yuan, Z. J. Yu and E. R. Bernstein, *J. Chem. Phys.* **140**, 074708 (2014).
46. E. J. Reed, M. R. Manaa, L. E. Fried, K. R. Glaesemann and J. D. Joannopoulos, *Nat. Phys.* **4**, 72 (2008).
47. A. F. Goncharov, M. R. Manaa, J. M. Zaug, R. H. Gee, L. E. Fried and W. B. Montgoery, *Phys. Rev. Lett.* **94**, 065505 (2005).
48. M. R. Manaa and L. E. Fried, *J. Phys. Chem. C* **116**, 2116 (2012).
49. F. H. Allen, C. A. Baalham, J. P. M. Lommerse, P. R. Raithby and E. Sparr, *Acta Cryst.* **B53**, 1017 (1997).
50. L. A. Curtiss, K. Raghavachari, P. C. Redfern and J. A. Pople, *J. Chem. Phys.* **106**, 1063 (1997).
51. M. W. Chase, C. A. Davies, J. R. Downey, D. J. Frurip, R. A. McDonald and A. N. Syverud, *J. Phys. Chem. Ref. Data* **14**, 1-926 (1985).
52. L. Maschio, B. Civalleri, P. Ugliengo and A. Gavezzotti, *J. Phys. Chem. A* **115**, 11179 (2011).
53. A. Otero-de-la-Roza and E. R. Johnson, *J. Chem. Phys.* **137**, 054103 (2012).
54. A. M. Reilly and A. Tkatchenko, *J. Chem. Phys.* **13**, 024705 (2013).